

Wavelength Scaling and Square/Stripe and Grain Mobility Transitions in Vertically Oscillated Granular Layers

Paul B. Umbanhowar^{a,1} and Harry L. Swinney^{b,2}

^a*Department of Physics and Astronomy, Northwestern University
Evanston, IL 60208*

^b*Center for Nonlinear Dynamics and Department of Physics
The University of Texas at Austin
Austin, TX 78712*

Abstract

Laboratory experiments are conducted to examine granular wave patterns near onset as a function of the container oscillation frequency f and amplitude A , layer depth H , and grain diameter D . The primary transition from a flat grain layer to standing waves occurs when the layer remains dilated after making contact with the container. With a flat layer and increasing dimensionless peak container acceleration $\Gamma = 4\pi^2 f^2 A/g$ (g is the acceleration due to gravity), the wave transition occurs for $\Gamma \approx 2.6$, but with decreasing Γ the waves persist to $\Gamma = 2.2$. For $2.2 < \Gamma < 3.8$, patterns are squares for $f < f_{ss}$ and stripes for $f > f_{ss}$; H determines the square/stripe transition frequency $f_{ss} = 0.33\sqrt{g/H}$. The dispersion relations for layers with varying H collapse onto the curve $\lambda/H = 1.0 + 1.1(f\sqrt{H/g})^{-1.32 \pm 0.03}$ when the peak container velocity $v = 2\pi A f$ exceeds a critical value, $v_{gm} \approx 3\sqrt{Dg}$. Local collision pressure measurements suggest that v_{gm} is associated with a transition in the horizontal grain mobility: for $v > v_{gm}$, there is a hydrodynamic-like horizontal sloshing motion, while for $v < v_{gm}$, the grains are essentially immobile and the stripe pattern apparently arises from a bending of the granular layer. For f at v_{gm} less than f_{ss} and $v < v_{gm}$, patterns are tenuous and disordered.

PACS numbers: 83.10.Pp, 47.54.+r, 83.10.Ji, 81.05.Rm

Keywords: pattern, granular media, bifurcation, wavelength

¹ email: umbanhowar@nwu.edu

² email: swinney@chaos.ph.utexas.edu

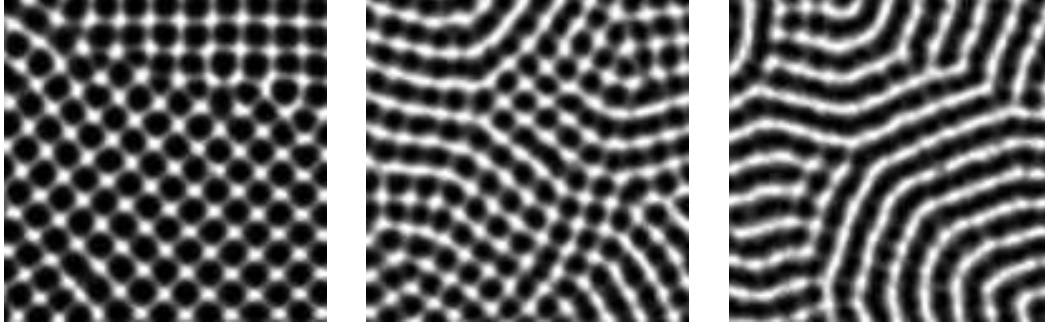


Fig. 1. Images of granular wave patterns near onset: (left) squares, $f = 33$ Hz ($f^* = 0.28$), (center) squares and stripes, $f = 37$ Hz ($f^* = 0.31$), and (right) stripes, $f = 43$ Hz ($f^* = 0.36$). In each case $D = 0.17$ mm bronze, $\Gamma = 2.5$, $N = 4$, container is $S1$, and the image size is 40.5×40.5 mm.

1 Introduction

Granular materials are collections of discrete solids for which even the simplest realizations — ensembles of identical solid spheres interacting only via contact forces — exhibit a wealth of surprising behaviors [1]. Our work on granular media has focused on a dynamic phenomenon, the formation of subharmonic standing waves in vertically oscillated granular layers [2,3]. These strongly nonlinear waves form patterns of stripes, squares, hexagons and more complex patterns [4], as well as localized structures called oscillons [5], as a function of three dimensionless control parameters: the acceleration Γ , the frequency $f^* = f\sqrt{H/g}$, and the layer thickness $N = H/D$. This paper concerns the square or stripe patterns that arise at the primary instability as Γ is increased; examples of these patterns are shown in Fig. 1. Despite being composed of discrete grains and having typical wavelengths λ of only 20-30 D , the appearance of granular patterns is similar to that of patterns in fluid systems [6,7], the closest example being standing surface waves in a vertically oscillated liquid layer (the Faraday instability) [8].

Pattern formation in granular media can perhaps be described by continuum equations analogous to those used in fluid system [9–11], but the continuum equations remain largely untested by experiment. Aspects of granular patterns have been described using phenomenological models [12–14], but making the connection to real systems requires an understanding of granular media at a more microscopic level. Recently, molecular dynamics simulations have begun to yield new details concerning the behavior of granular waves [15]. In particular, a simulation developed by Bizon *et al.* [16] quantitatively reproduces the granular patterns observed in three dimensions and thus allows calculation of quantities not readily accessible by experiment.

In this paper, we will first describe our experimental system and then discuss

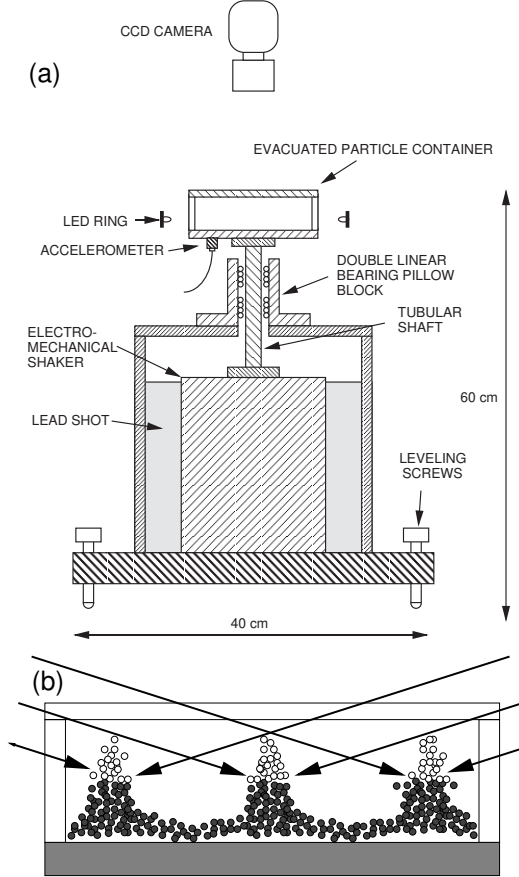


Fig. 2. (a) Experimental apparatus and (b) lighting. Patterns are illuminated from the side by light incident at low angles; high regions are bright and low regions are dark.

some generic features of the flat-layer/wave transition. Next, we will present results for the scaling of the square/stripe transition frequency and the wavelength with particle size and layer depth. Last, we will use results from local measurements of the collision pressure and from dispersion relations to demonstrate and characterize the grain mobility transition.

2 Experiment

Our experimental apparatus is similar to that used in Refs. [3–5] and is described in detail in Ref. [17]. A layer of granular material is placed in the bottom of an evacuated container mounted on the armature of an electro-mechanical shaker and sinusoidally oscillated in the vertical direction (see Fig. 2(a)). Our granular layers consist of spherical non-cohesive and non-magnetic particles of bronze, 316 stainless steel, titanium, or lead with as-poured densities of 5.1, 2.6, 4.7 and 6.7 g/cm³ respectively, and with $0.05 < D < 0.8$ mm and a poly-dispersity of $\pm 10\%$. Data is obtained for $D = 0.17$

Table 1
Container specifications.

Container	Shape	Size (mm)	Base (mm)	Mass (g)
<i>C</i>	circular	126 (dia.)	10.2	1150
<i>S1</i>	square	162 (side)	12.7	2170
<i>S2</i>	square	106 (side)	12.7	1460

mm bronze particles except as noted. Three different containers are used (see Table 1); each has a polished aluminum base to prevent static charge accumulation and clear plastic side walls and top for lighting and visualization respectively. An accelerometer mounted on the underside of the container measures the acceleration. The patterns are visualized using as a light source a ring of strobed light-emitting diodes, which encircle the container and illuminate the layer from the side (Fig. 2(b)). Images are acquired by a digital CCD camera mounted on axis.

The momentum transfer generated during layer-container contact is measured by an acceleration compensated pressure sensor with a resonant frequency of 300 kHz (PCB 112A22). This sensor has a circular sensing area 5.5 mm in diameter; the sensor size can be compared with the wavelength of the pattern, which varies from 2 to 40 mm for the present measurements, and the particle size, typically 0.17 mm. The sensor is flush mounted (± 0.02 mm) 13 mm from one container sidewall and 36 mm from the other in the bottom of cell *S2*. To avoid high sampling frequencies, a circuit consisting of a peak detector, a level shifter, and a sample-and-hold is used to record the maximum pressure from each collision of the layer with the container.

3 Wave Onset

Here we investigate the transition from a flat layer to standing waves in the regime where the layer free-flight time t_{flt} is less than one period of oscillation of the container T . The layer state is characterized by local collision pressure measurements [18]. Related work is reported in Ref. [17] and in Refs. [19,20], where in the latter, global force and optical measurements characterize the flat layer state. For $\Gamma < 1$, the layer is always in contact with the plate and there is no significant relative grain motion. For $\Gamma > 1$, we identify three distinct stages of layer motion during each cycle: free-flight – layer not in contact with container; impact – layer and container collide; contact – layer and container in contact and moving with the same vertical velocity. Impact imparts relative kinetic energy to the grains which, if large enough, enables the layer to change its configuration.

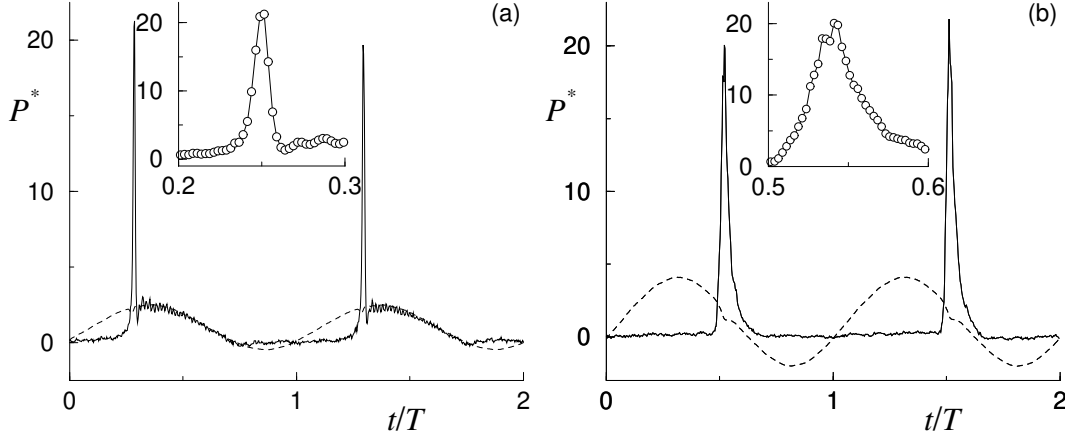


Fig. 3. Non-dimensionalized layer pressure for (a) $\Gamma = 1.5$ (flat layer) and (b) $\Gamma = 3.1$ (waves) with $f^* = 0.48$ ($f = 40$ Hz) and $N = 9$. Dashed curve is a plot of $a(t)/g + 1$. The insets show expanded portions of the collision region and illustrate the increase in collision time associated with waves onset.

We first describe some generic features of the layer-container pressure in the vicinity of the flat-layer/waves transition. A time series for the local pressure exerted by the granular layer on the container below the onset of the waves is plotted in Fig. 3(a). The pressure is expressed in non-dimensional form, $P^* = P/\rho g H$, where P is the pressure and ρ is the as-poured layer density. $P^* = 0$ indicates the layer is in free-flight, the sharp jump in P^* occurs at impact, while contact is shown by $P^* \approx a(t)/g + 1$ — the pressure calculated using the measured plate acceleration and assuming a solid layer attached to the plate (dashed curve). Several features of P^* should be noted. As the inset in Fig. 3(a) emphasizes, the collision duration is short, less than $0.02T$, which indicates the layer is relatively compact at the time of collision. Furthermore, immediately following the collision, $P^* = a(t)/g + 1$, which shows the collision is strongly inelastic (if the layer bounced, P^* would be reduced). Finally, P^* and $a(t)/g + 1$ go to zero simultaneously, which indicates the entire layer is moving upward with the container velocity when free-flight begins.

To contrast the layer behavior above and below wave onset, a time series of P^* in the wave regime is presented in Fig. 3(b). Here the layer motion consists of just two stages, a free-flight followed by an extended collision. There is no longer a contact stage as indicated by the observation that P^* is always larger than $a(t)/g + 1$, and that $a(t)/g + 1$ goes to zero before P^* goes to zero. From these observations, we infer that the layer is expanded at impact, that at no time during the collision is the entire layer totally at rest with respect to the container, and that the collision continues for a short time after $a(t)$ becomes less than g .

At the onset of waves, the maximum collision pressure per cycle, P_{max}^* , decreases rapidly, as Fig. 4(a) illustrates. This decrease is associated with an increase in layer dilation (see Fig. 3). With increasing Γ , the decrease in P_{max}^*

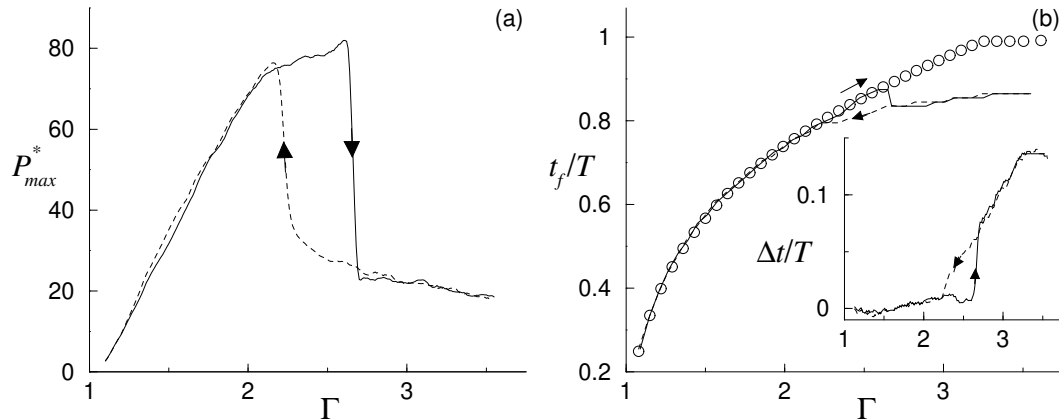


Fig. 4. The hysteresis in the transition from a flat layer to waves is revealed in measurements of (a) maximum collision pressure and (b) dimensionless flight time versus acceleration amplitude for increasing (solid-line) and decreasing (dashed-line) Γ ($f = 26$ Hz ($f^* = 0.31$), $N = 8.2$). The inset in (b) plots the difference Δt between the flight time calculated from the inelastic layer model (\circ in (b)) and the experimental flight time. Experimental data are averaged into 0.01 intervals in Γ and averaged over approximately 20 full ramps of Γ .

occurs at $\Gamma = 2.7$. However, the transition is hysteretic and the layer reverts to the flat state at $\Gamma = 2.2$, where P_{max}^* increases abruptly (see Fig. 4(a)). For the flat layer, P_{max}^* increases with increasing Γ , while in the wave state, P_{max}^* decreases with increasing Γ [21]. Additional measurements using steel and titanium particles show a somewhat different behavior [17]. Before the transition to waves ($\Gamma \approx 1.9$), P^* in these larger restitution coefficient materials drops from 80 to approximately 40 but then continues to increase until the onset of waves at which point P^* drops to 20 as for the bronze layers.

Figure 4(b) compares the layer free-flight time measured from the experiment with the time calculated from the completely inelastic layer model [22,3]. When the layer is flat, the measured and calculated flight times are nearly identical. However, when waves arise, the measured flight time is smaller than the model predicts (see inset in Fig. 4(b)). This discrepancy arises because the velocity of a portion of the layer is less than the container velocity when $a(t)$ becomes less than g . These slower grains reduce the effective layer take-off velocity, which decreases t_{flt} . For increasing Γ , there is a sudden decrease in t_{flt} when waves arise. However, for decreasing Γ , and unlike P_{max}^* , t_{flt} continuously decreases until it equals the model value at which point the layer reverts to the flat state. The equality of measured and model values of t_{flt} at this transition implies that for waves to exist, a portion of the layer must be dilated when the bottom of the layer leaves the container. This necessary condition appears to be due to the strongly dissipative nature of the granular layer, which rapidly removes kinetic energy when layers remain in contact with the container.

The qualitative features of the transition from a flat layer to waves, shown in

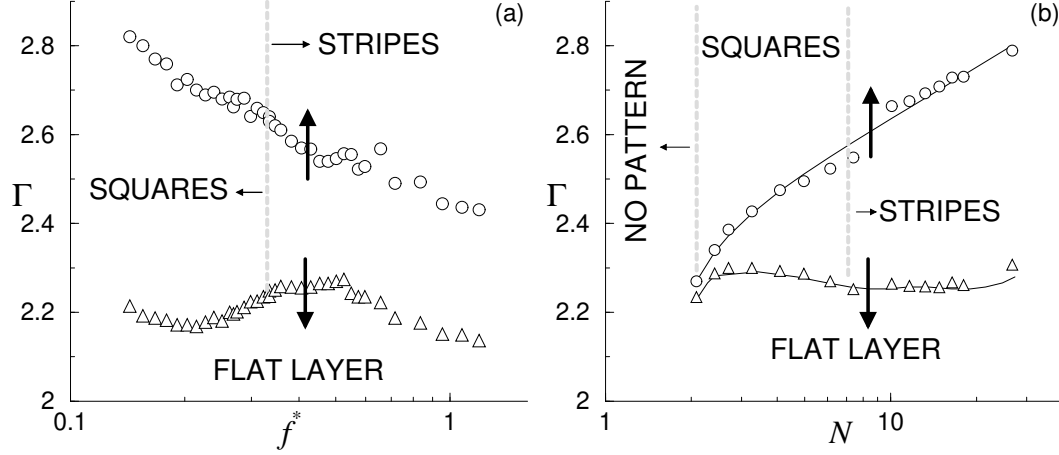


Fig. 5. Stability diagram showing pattern transitions with increasing (\circ) and decreasing (\triangle) Γ as a function of (a) f^* with dimensionless layer thickness $N = 9$, and (b) N with $f^* = 0.36$ ($f = 30$ Hz). Hysteresis decreases with increasing f^* and increases with increasing N . In (b) for $N \lesssim 2$ the hysteresis vanishes; as Γ is increased in this regime the layer dilates into a uniform low density gas-like state.

Figs. 3 and 4, are the same for the entire range of H , D , and f we examine. However, other features of the transition are non-trivial functions of H and f . For instance, the Γ value at which the transition from a flat layer to waves occurs, Γ_c , is plotted in Fig. 5(a) as a function of f^* . For increasing Γ , $\Gamma_{c\uparrow}$ decreases monotonically with f^* , while for decreasing Γ , $\Gamma_{c\downarrow}$ is nearly constant except for a slight local increase near $f^* \approx 0.4$ [23]. The observation that the existence of waves depends on the layer never reaching the contact stage gives the following necessary condition for wave existence

$$T - t_{flt} = t_{coll} = h/v_{coll}, \quad (1)$$

where h is the layer dilation (actual layer thickness minus H), t_{coll} is the collision duration, and v_{coll} is the collision velocity. At the flat-layer/waves transition for decreasing Γ , $\Gamma_{c\downarrow}$ is nearly constant which implies $h \propto f^{-2}$ since $T - t_{flt}$ and v_{coll} are both proportional to f^{-1} . For the data in Fig. 5(a), $\Gamma_{c\downarrow} \approx 2.2$ which gives $h = 0.25v_{coll}t_{flt}$. Similarly, applying Eq. (1) in the flat layer regime where $\Gamma_{c\uparrow}$ is a function of f , yields $h \propto f^{-1.8}$ — a slower decrease with increasing f than for waves.

Γ_c is also a function of N , as Fig. 5(b) shows. $\Gamma_{c\downarrow}$ is nearly independent of N , while $\Gamma_{c\uparrow}$ is roughly proportional to N . The transition as measured by the rapid drop in P_{max} is no longer subcritical for $N \lesssim 2$ — the same N value below which coherent wave patterns disappear. Interpreting these results in light of Eq. (1), the increase in $\Gamma_{c\uparrow}$ with increasing N is due to the greater dissipation in the thicker layer which reduces h . The disappearance of waves for $N \leq 2$ is likely a result of large grain velocity fluctuations that destroy coherent layer motion. This interpretation is also supported by experiments

with different materials [17]: materials with a restitution coefficient larger than that of bronze, such as stainless steel and titanium, require deeper layers than does bronze to generate waves. Lead, which has a smaller restitution coefficient than bronze, requires a layer of only $N = 1.1$ for waves to exist. Additionally, in layers deep enough to form waves, we find that higher (lower) restitution materials have higher (lower) values of Γ_c for equal N .

In Ref. [16], Bizon *et al.* note that waves in their simulations form when the time for peak growth is greater than that for peak decay. From this observation, they calculate $\Gamma_{cl} \approx 2.47$ independent of either f , D , or H . The data presented above is in reasonable agreement with their prediction. Their observation does not address the internal layer state and thus can not predict the value of Γ_{cl} and its dependence on f and N . With results from simulations, it will be possible to measure h and thus check the validity of the criteria for wave onset proposed in Eq. 1.

4 Square/Stripe Transition

The wave patterns at the primary bifurcation are squares for low f^* and stripes for high f^* , while for intermediate f^* , both patterns are observed simultaneously (see Fig. 1). To quantify the square/stripe transition, we divide the pattern images into $3\lambda \times 3\lambda$ regions, calculate the spatial power spectra, radially average the power within one full width at half maximum of the dominant wavenumber, and subtract the mean to obtain $I(\theta)$. The autocorrelation function $C(\pi/2) = \langle I(\theta)I(\theta + \pi/2) \rangle_\theta / \langle I^2(\theta) \rangle_\theta$ is then used to characterize the pattern. For perfect squares $C(\pi/2) = 1$, whereas for an image of perfect stripes $C(\pi/2) = 0$. Differences between the measured and ideal values (*i.e.*, $C(\pi/2) < 0$) are due to the finite angular width of the spectral peak. Figure 6 is a plot of $C(\pi/2)$ versus f^* , which shows the transition from squares to stripes occurs in a narrow frequency range about the transition frequency $f_{ss}^* = 0.31$, with $C(\pi/2)$ nearly constant above and below f_{ss}^* . The value of f_{ss}^* is not sensitive to details of the method: plotting $I(\theta_{max} \pm \pi/2)$, where θ_{max} is the azimuthal location of the maximum value of $I(\theta)$, as well as varying the sub-image size, yield the same result.

Figure 7(a) is a plot of f_{ss}^* as a function of Γ for fixed N . There is little change in f_{ss}^* as Γ is increased from near wave onset to close to the transition to hexagons [3]. Figure 7(b) plots f_{ss}^* against N . Although N varies by more than an order of magnitude, the non-dimensionalized square/stripe transition frequency remains nearly fixed. Included in Fig. 7(b) are additional measurements that indicate f_{ss}^* also does not depend strongly on D , material, or container size or shape.

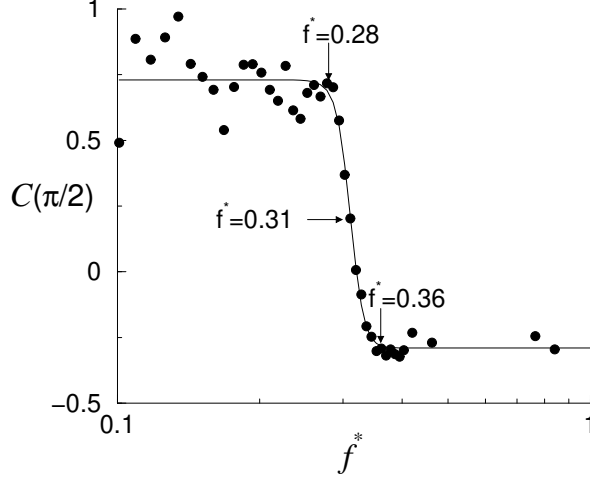


Fig. 6. The transition from square patterns at low frequencies to stripe patterns at high frequencies is indicated by the decrease in the autocorrelation function of radially averaged power spectral density at $\theta = \pi/2$ ($\Gamma = 2.5$, $N = 4$, $S1$). The solid line is a fit to $a + b \tanh[c(f^* - f_{ss}^*)]$ with $f_{ss}^* = 0.31$. The labeled f^* values correspond to the images in Fig. 1.

Bizon *et al.* have proposed that the square/stripe transition occurs when the distance that the layer falls from its maximum height to the container is equal to the layer depth: for fall distances larger (smaller) than H , squares (stripes) are the preferred pattern [16]. Using a simple model that considers the layer as a totally inelastic object with no internal modes [22,3], they calculate $f_{ss}^* = 1/\sqrt{8} \approx 0.35$. The data presented here gives an average value of $f_{ss}^* \approx 0.33$ over a large range of experimental parameters. The preceding measurements as well as the criterion of Bizon *et al.* suggest that the square/stripe transition

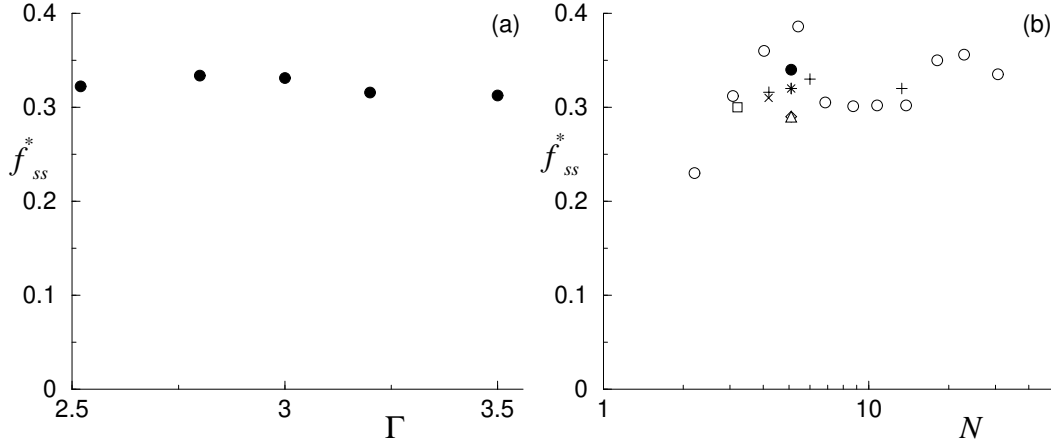


Fig. 7. (a) Square/stripe transition frequency as a function of Γ for $N = 13$ (container $S1$). (b) Square/stripe transition frequency as a function of N : \circ ($\Gamma = 3.0$, 0.17 mm, C), $+$ ($\Gamma = 2.5$, 0.17 mm, $S1$), \times ($\Gamma = 3.1$, 0.66 mm, $S1$), \square ($\Gamma = 2.5$, 0.46 mm lead, C), $*$ ($\Gamma = 3.0$, 0.07 mm, C), \bullet ($\Gamma = 3.0$, 0.78 mm, C), \diamond ($\Gamma = 2.8$, 0.17 mm steel, C), \triangle ($\Gamma = 2.8$, 0.17 mm titanium, C).

is primarily a function of the layer depth H . Layers with differing N and D but equal H make the transition from squares to stripes at the same f (except for layers with $N \sim O(1)$ where the pattern weakens due to large relative particle velocities). This result implies that the layer acts as a continuum, *i.e.*, the size of the particles does not affect the bulk behavior although the discrete nature does. In contrast, the dependence of the critical acceleration amplitude for waves on N and f , where scaling with H fails (Fig. 5(b)), suggests that the physics determining subcriticality and square/stripe pattern selection are unrelated.

5 Wavelength Scaling

The dispersion relation for surface waves in inviscid fluids in the absence of surface tension and in the shallow water limit ($\lambda > H$) is $\lambda/H = f^{-1}\sqrt{g/H}$. When plotted in this form, which uses H and $\sqrt{H/g}$ as the characteristic length and time scales respectively, the dispersion relations for different depth layers lie on a single curve. In granular layers, however, there are two natural length scales – layer depth and grain diameter. We show in this section that below a critical frequency, wavelength scaling is governed by H as is the case for fluids, while above this frequency, scaling with H fails. In the next section (Sec. 6), we will show that the scaling breakdown is associated with a transition in the horizontal grain mobility.

Figure 8(a) presents results for the wavelength as a function of frequency

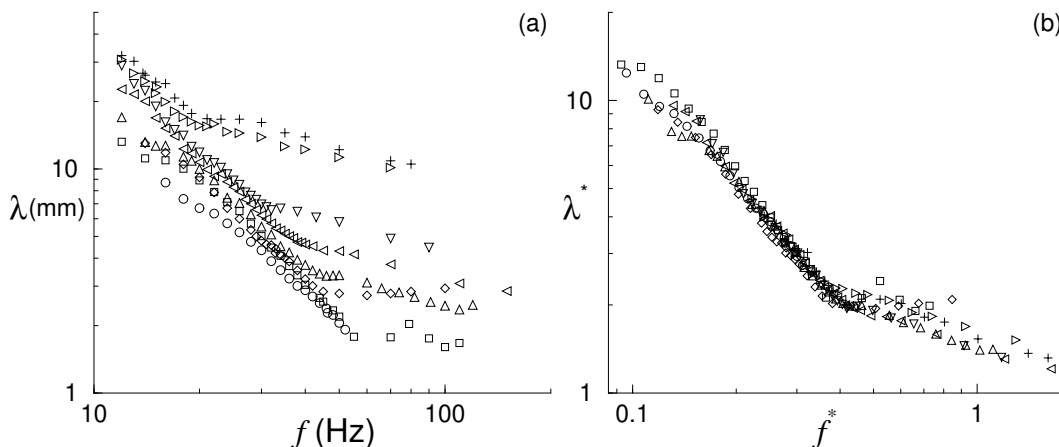


Fig. 8. Wavelength as a function of frequency for layers of constant dimensionless depth $N = H/D$ and varying particle diameter D . (a) λ versus f for 0.07 mm (\circ), 0.08 mm (\square), 0.14 mm (\diamond), 0.17 mm (\triangle), 0.23 mm (\triangleleft), 0.33 mm (∇), 0.66 mm (\triangleright), and 0.78 mm ($+$) ($\Gamma = 3.0$, $N = 5$, SI). (b) Same data plotted with dimensionless variables using H as the fundamental length scale. Near $f^* = 0.4$ in (b), there is a kink in the dispersion curve, which moves to higher f^* as N is increased.

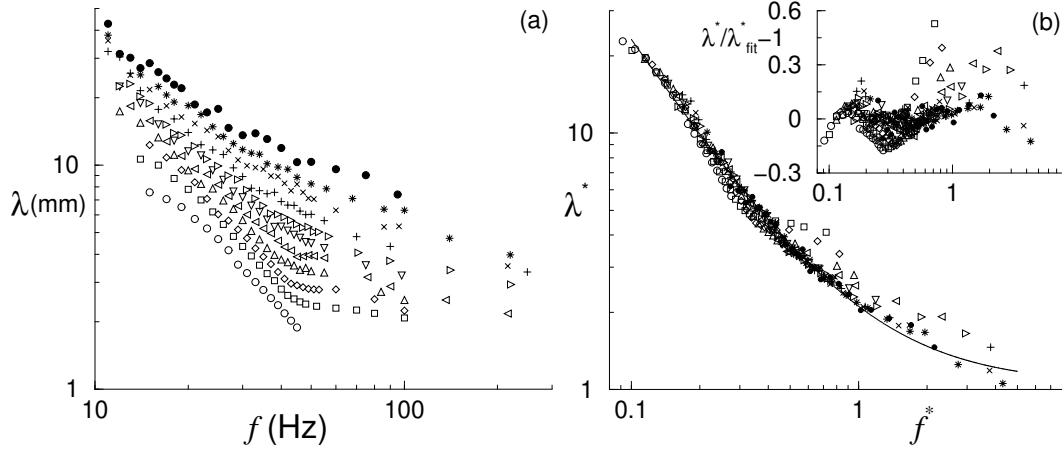


Fig. 9. Dispersion relation for layers of constant particle diameter and varying dimensionless depth, $N = H/D$: (a) Wavelength as a function of frequency: $N = 2.2$ (\circ), $N = 3.1$ (\square), $N = 4.0$ (\diamond), $N = 5.4$ (\triangle), (\triangleleft) $N = 6.8$, $N = 8.7$ (\triangleright), $N = 10.7$ (\triangleright), $N = 13.8$ (+), $N = 18.1$ (\times), $N = 22.8$ (*), and $N = 30.7$ (\bullet) ($D = 0.17$ mm, $\Gamma = 3.0$, container C). (b) Same data plotted with dimensionless variables. The dimensionless data in (b) are fit to Eq. 2; the inset shows the residuals. As N increases, the f^* range over which data collapse occurs increases.

for layers of bronze particles with $N = 5$, $\Gamma = 3.0$, and a range of particle sizes ($0.07 < D < 0.8$ mm). The wavelength decreases with increasing f and increases with increasing D . When H is used to non-dimensionalize the wavelength $\lambda^* = \lambda/H$ and the frequency $f^* = f\sqrt{H/g}$, the data collapse onto a single curve (Fig. 8(b)). A well-defined kink in the dispersion curve occurs near $f^* = 0.4$, above which λ^* decreases more slowly with increasing f^* . A similar slowing has been observed in other experiments but only for one [24] and two [16] disjoint values of D .

Because N is constant for the data presented in Fig. 8, it is unclear whether H or D is the length scale governing the collapse since $H = ND$. To test whether the data collapse obtained in Fig. 8(b) is due to scaling with H , we plot in Fig. 9 the wavelength versus frequency with fixed $D = 0.17$ mm but with N varying from 2 to 31. λ increases with increasing H and again the unscaled data collapse when λ^* is plotted as a function of f^* . Similar results were obtained by Bizon *et al.* but only for two values of N ($N = 2.7, 5.4$) [16].

The rescaled data in Fig. 9(b) fit the functional form $\lambda^* = a + bf^{*c}$ with the best fit given by

$$\lambda^* = 1.0 + 1.1f^{*-1.32 \pm 0.03}. \quad (2)$$

The residuals from the fit to the rescaled dispersion data in Fig. 9(b) (see inset) for $f^* \geq 0.4$ exhibit a marked decrease in the quality of the data collapse, which is a function of H and which is characterized by a slowing in the decrease of

λ^* with increasing f^* . This slowing is more pronounced in small N layers. We will return to this observation in the next section.

Three points should be noted concerning the dispersion relation data. First, although the granular data collapse below the kink in the dispersion curves when scaled with H as for fluid surface waves, the dispersion relations for these two media are different. Second, the exponent in Eq. 2 is not equal to -2 as was found in our earlier work on glass beads in air [2], by Metcalf *et al.* [24] for glass beads in an evacuated container, and by Clément *et al.* in a two-dimensional layer of aluminum balls [25]. Possible explanations for the larger value of exponent found in the other studies include the influence of air viscosity, static charging in non-conducting grains, small aspect ratios, and drag associated with the side walls. Finally, the fit predicts a minimum wavelength equal to H for large f . The $\lambda^* = 1$ limit is clearly unattainable in small N layers due to the finite size of the layer's constituent grains; thus, scaling with H will fail for small N . However, as we will show next, breakdown of scaling normally occurs before this limit is reached due to a reduction in the grain mobility.

6 Grain Mobility Transition

As discussed in the previous two sections, the layer depth is the characteristic length scale which determines the scaling properties of the square/stripe transition and the wavelength. However, as mentioned in Secs. 1 and 5, the grain diameter D is also expected to influence the layer response. Consider the initial velocity required to raise a grain a distance D in the presence of gravity, $v_D = \sqrt{2gD}$. If the grain is embedded in a plane of identical particles, horizontal motion will only be possible if $v_D > \sqrt{2gD}$; for lower velocities, the grain will be stuck. Assuming further that the fluctuation velocity of a typical grain with respect to its neighbors is proportional to the peak container velocity $2\pi Af$, a relevant dimensionless parameter characterizing grain mobility is $\tilde{v} = 2\pi Af / \sqrt{Dg}$. Section 6.1 presents evidence of a qualitative change in the layer response at a particular value of \tilde{v} which we call the grain mobility transition, $\tilde{v}_{gm} \approx 2.5$, for large Γ or small N . Section 6.2 then shows that this change appears related to the loss of horizontal grain mobility for $\tilde{v} < \tilde{v}_{gm}$.

6.1 Changes in Layer Response

The value of f^* below which data collapse occurs for constant D and varying N is marked by a kink in the dispersion curves (see Fig. 9(b)) and is an increasing function of N . The data in Fig. 8(b) for constant N and varying D show a

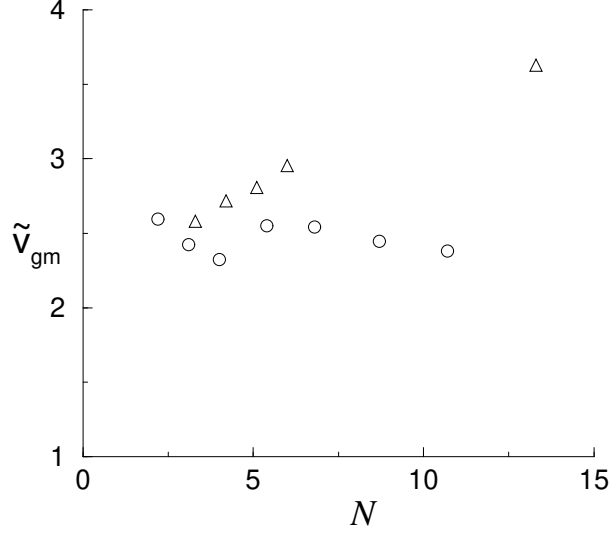


Fig. 10. Dimensionless container velocity at which λ^* begins to decrease slower than Eq. 2, as a function of N for the data in Fig. 9(b) with $\Gamma = 3.0$ (\circ) and for additional data [17] with identical particles but with $\Gamma = 2.5$ (\triangle). For $\Gamma = 3.0$, \tilde{v}_{gm} is nearly constant, while for $\Gamma = 2.5$, \tilde{v}_{gm} increases gradually with increasing N .

similar kink which is, in contrast to the data for constant D , independent of H for fixed N . To characterize the location of the kink, Fig. 10 presents a plot of \tilde{v} at the kink (*e.g.* \tilde{v}_{gm}) as a function of N for $\Gamma = 3.0$ and $\Gamma = 2.5$ [26]. For $\Gamma = 3.0$, $\tilde{v}_{gm} \approx 2.5$ and shows no systematic dependence on N . This is nearly the same as $\tilde{v}_{gm} = 2.6$, the value found for varying D , constant $N = 5$ and $\Gamma = 3.0$ (see Fig. 8). For $\Gamma = 2.5$, \tilde{v}_{gm} is slightly larger and is a slowly (slower than \sqrt{N}) increasing function of N .

To summarize, for $v > v_{gm}$, λ^* is independent of H and scales with f^* , while for $v < v_{gm}$, λ^* scaling with H fails. This breakdown appears to be related to a transition in the layer response when \tilde{v} is small. Observations at $\tilde{v} \approx 0.5$ using relatively large grains show that there is little if any horizontal particle motion at the surface. In contrast, for $\tilde{v} > \tilde{v}_{gm}$, grains slosh back and forth – in thinner layers ($N \approx 4$) the sloshing is so vigorous that the layer depth goes to zero in the pattern minima. To illustrate the difference between these two wave regimes, Fig. 11 presents a plot of λ^* versus \tilde{v} for $N = 5$ and $\Gamma = 2.5$ and $\Gamma = 3.0$. The wavelength is approximately 10 percent larger for $\Gamma = 2.5$ than for $\Gamma = 3.0$ when $\tilde{v} > \tilde{v}_{gm} \approx 2.6$, but for $\tilde{v} < \tilde{v}_{gm}$, λ^* for $\Gamma = 2.5$ jumps to 1.5 times λ^* for $\Gamma = 3.0$. If λ^* is instead plotted versus f^* , the change in behavior is even more evident: for f^* below the transition λ^* increases with increasing Γ , while for f^* above, λ^* decreases with increasing Γ .

In addition to the breakdown in λ scaling with H , a qualitative change in the collision pressure is also observed for $\tilde{v} \approx 3$. The \tilde{v} dependence of the Γ averaged collision pressure $\langle P_{max}^* \rangle_\Gamma = \int_{\Gamma_{min}}^{\Gamma_{max}} P^*(\Gamma) d\Gamma$ is plotted in Fig. 12

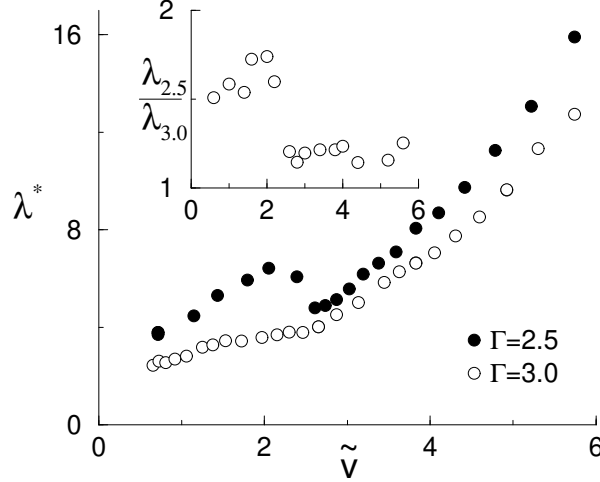


Fig. 11. $\lambda^* = \lambda/H$ versus $\tilde{v} = 2\pi Af/\sqrt{Dg}$ for $\Gamma = 2.5$ (●) and $\Gamma = 3.0$ (○) (0.46 mm lead, $N = 5$, container C). Inset: The λ ratio jumps for $\tilde{v} < 2.6$, which indicates the grain mobility transition.

for both the flat-layer and wave regimes. For the flat layer, $\langle P_{max}^* \rangle_\Gamma$ increases continuously with increasing v . However, in the wave regime $\langle P_{max}^* \rangle_\Gamma$ is nearly constant for $\tilde{v} > 3$ but decreases in a similar fashion to the flat layer for $\tilde{v} < 3$ [27]. The latter result suggests that the flat layer and wave states are similar for $\tilde{v} < 3$ as would be expected below the grain mobility transition.

Finally, as Sec. 4 describes, the frequency of the square stripe transition is given by $f_{ss} = 0.33\sqrt{g/H}$ and shows no systematic dependence on the grain size. However, in thin layers when $\Gamma\sqrt{N} < 2\pi\tilde{v}_{gm}f_{ss}^*$, the frequency associated with the grain mobility transition f_{gm} is less than the frequency of the square/stripe transition. In this case and for $\tilde{v} \lesssim \tilde{v}_{gm}$, the resulting wave patterns are noticeably more tenuous and have significantly shorter spatial correlation lengths (on the order of λ) than do the corresponding patterns for $f_{ss} > f_{gm}$.

6.2 Loss of Horizontal Grain Motion

In this section, the breakdown in λ scaling with H and the decrease in the collision pressure are identified with a transition in the horizontal grain mobility. We present data suggesting that for $\tilde{v} > \tilde{v}_{gm}$, the local layer height is changed by lateral grain motion, while for $\tilde{v} < \tilde{v}_{gm}$, grains are essentially immobile [28]. In Ref. [20], Mujica and Melo similarly propose that waves at low container velocities result from bending of the layer and not from horizontal grain transfer. Also, in our direct visual observations we observe significant horizontal particle motion for waves at large \tilde{v} but no noticeable horizontal grain motion for waves at small \tilde{v} . In general for waves at both high and

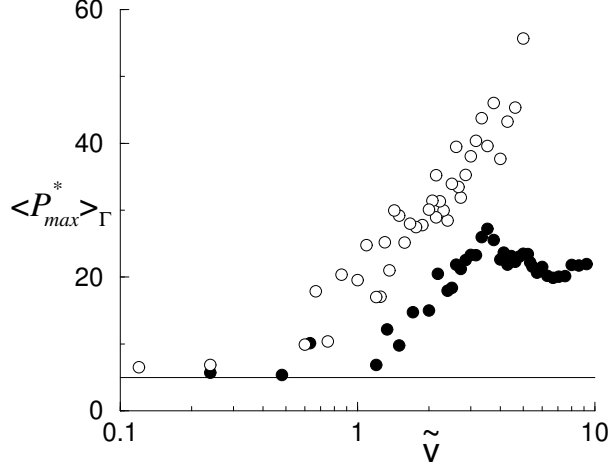


Fig. 12. Γ -averaged collision pressure versus container velocity below wave onset for $1.2 < \Gamma < 1.8$ (\circ) and above wave onset for $2.8 < \Gamma < 3.2$ (\bullet) ($N = 9$). For $\tilde{v} > 3$, $\langle P_{max}^* \rangle_\Gamma$ in the wave regime is constant, while for $\tilde{v} < 3$, $\langle P_{max}^* \rangle_\Gamma$ for waves and flat-layer show similar behavior. The line at $\langle P_{max}^* \rangle_\Gamma = 5$ represents the calculated minimum value for P_{max}^* at $\Gamma = 3.0$.

low \tilde{v} , patterns persist when the container is rapidly brought to rest. When the stationary container is lightly and repeatedly tapped, the patterns at low \tilde{v} slowly disappear without any apparent grain motion on the layer surface, whereas the high \tilde{v} patterns exhibit significant grain rearrangement.

To quantitatively investigate the proposed grain mobility transition, fluctuations in the local collision pressure are studied. In the presence of waves and for $\tilde{v} > \tilde{v}_{gm}$, relatively large fluctuations in the collision pressure associated with changes in the local layer height due to grain motion are expected. Conversely, for $\tilde{v} < \tilde{v}_{gm}$ fluctuations should be smaller because the layer height is essentially constant. Figure 13(a) plots the relative standard deviation of the maximum pressure $\sigma_{P_{max}} = \sqrt{(\Delta P_{max})^2} / \langle P_{max} \rangle$ versus \tilde{v} for both the flat-layer and wave regimes where $\sqrt{(\Delta P_{max})^2}$ and $\langle P_{max} \rangle$ are the standard deviation and mean of P_{max} respectively. For the flat-layer, $\sigma_{P_{max}}$ is small and nearly independent of \tilde{v} . For the wave regime, $\sigma_{P_{max}}$ shows three distinct behaviors — $\tilde{v} < 3$: $\sigma_{P_{max}}$ is independent of \tilde{v} and equal to the flat-layer value; $3 < \tilde{v} < 7$: $\sigma_{P_{max}}$ increases with increasing \tilde{v} and is larger than the flat-layer value; $\tilde{v} > 7$: $\sigma_{P_{max}}$ decreases with increasing \tilde{v} .

As a further check that the equality of $\sigma_{P_{max}}$ for the flat-layer and waves for $\tilde{v} < 3$ is due to a loss of horizontal grain motion, Fig. 13(b) presents measurements of the autocorrelation of P_{max} at a delay of $4T$, $C_{P_{max}}(4T)$ [29]. $C_{P_{max}}(4T)$ is sensitive to periodic variations in P_{max} even when the intrinsic pressure noise is larger than the fluctuations associated with grain motion. As is true for $\sigma_{P_{max}}$, $C_{P_{max}}(4T)$ for the flat-layer is independent of \tilde{v} . For waves, the dependence of $C_{P_{max}}(4T)$ on \tilde{v} can also be divided into three regimes —

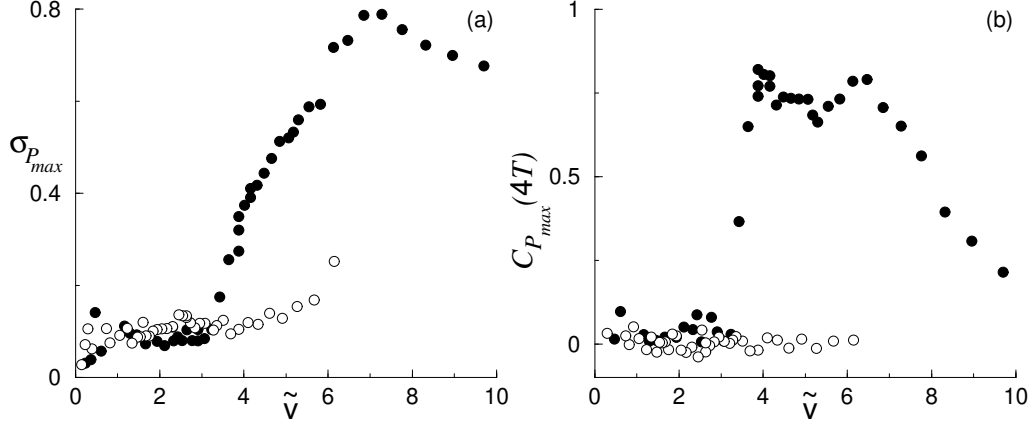


Fig. 13. Grain mobility below wave onset at $\Gamma = 1.9$ (\circ) and in wave regime at $\Gamma = 3.0$ (\bullet), characterized by (a) pressure fluctuations and (b) autocorrelation of peak pressure at a delay of $4T$ ($N = 9$). Near $\tilde{v} = 3$, both quantities change, which marks the grain mobility transition.

$\tilde{v} < 3$: $C_{P_{max}}(4T)$ is constant and equal to the flat-layer value; $3 < \tilde{v} < 7$: $C_{P_{max}}(4T)$ is constant and larger than the flat-layer value; $\tilde{v} > 7$: $C_{P_{max}}(4T)$ decreases with increasing \tilde{v} . The transition in $C_{P_{max}}(4T)$ to the flat-layer value is sharp and occurs at the same \tilde{v} where $\sigma_{P_{max}}$ for waves reaches its minimum value. Also, note that $\sigma_{P_{max}}$ peaks at the velocity ($\tilde{v} = 7$) at which $C_{P_{max}}(4T)$ begins to decrease for increasing \tilde{v} .

Our interpretation of the three regimes for $\sigma_{P_{max}}$ and $C_{P_{max}}$ shown in Fig. 13 is as follows. For $\tilde{v} < 3$ horizontal grain mobility is strongly reduced and the layer depth is everywhere equal. Waves in this regime are likely bending waves [20] since mass transfer, dilational waves [19], or any other mode giving rise to a periodic variation in pressure would produce positive correlations in the pressure fluctuations. For $\tilde{v} > 3$ waves are mass transfer waves. We speculate that the decrease in $\sigma_{P_{max}}$ and $C_{P_{max}}$ above $\tilde{v} = 7$ results from the disordered patterns found in this regime which possibly result from an instability associated with the more rapid growth of the wave amplitude in comparison to λ as f decreases [27].

Having made the case for a grain mobility transition in terms of $\sigma_{P_{max}}$ and $C_{P_{max}}$, we now examine the dependence of the transition on v , N , and D . Figure 14 presents $\sigma_{P_{max}}$ for varying Γ and nine distinct f values ranging from $0.05\sqrt{g/D}$ to $0.33\sqrt{g/D}$, as a function of \tilde{v} . Most importantly, Fig. 14 shows that variations in Γ at constant f produce the same changes in $\sigma_{P_{max}}$ as do variations in f at constant Γ (see Fig. 13(b)). This finding strengthens our proposition that $\tilde{v} = \Gamma/(2\pi f\sqrt{D/g})$ is the correct dimensionless parameter specifying the grain mobility. The data also show that $\tilde{v}_{gm} \approx 3$, which is in agreement with the value obtained from the pressure fluctuation data for $\Gamma = 3.0$.

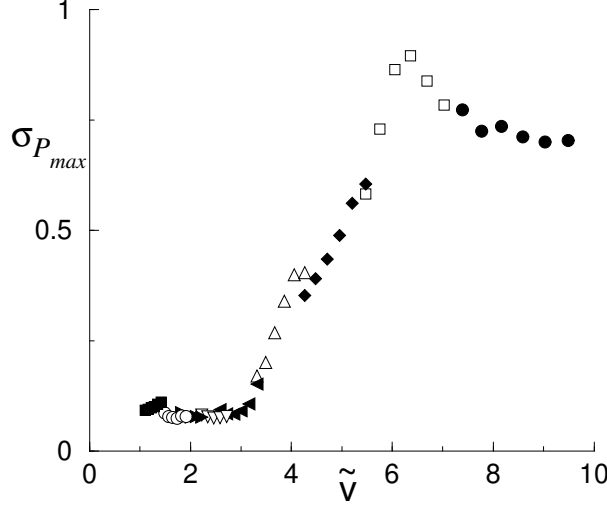


Fig. 14. Normalized collision pressure fluctuation in wave regime versus dimensionless peak container velocity for varying Γ and $f\sqrt{D/g} = 0.05$ (\bullet), 0.07 (\square), 0.09 (filled \diamond), 0.11 (\triangle), 0.14 (filled \triangleleft), 0.17 (∇), 0.21 (filled \triangleright), 0.25 (\circ), and 0.33 (filled \square) ($N = 9$). Note the similarity with Fig.13(a).

Figure 15(a) examines the dependence of grain mobility on layer depth by plotting $C_{P_{max}}(4T)$ versus N for $\tilde{v} = 3.4$ and $\tilde{v} = 4.2$. By choosing \tilde{v} slightly above $\tilde{v}_{gm} \approx 3$ (for $N = 9$), $C_{P_{max}}(4T)$ is sensitive to the grain mobility transition. Below $N = 14$, the layer response for the different \tilde{v} is similar. For $N < 5$, $C_{P_{max}}(4T)$ decreases to near 0 at $N \approx 2$, while for $5 < N < 14$, $C_{P_{max}}(4T)$ decreases slightly with increasing N . The dependence of $C_{P_{max}}(4T)$ on N at small N appears similar to that of $C_{P_{max}}(4T)$ on \tilde{v} at large \tilde{v} , suggesting that the two limits of large \tilde{v} and small N are related. For $N > 14$, $C_{P_{max}}(4T)$ continues to decrease slowly with increasing N for $\tilde{v} = 4.2$, but, for $\tilde{v} = 3.4$ and $N \geq 14$, $C_{P_{max}}(4T)$ drops to approximately the flat layer value. Possibly, the reduction in grain mobility with increasing N is due to a decrease in grain velocity associated with an increase in the grain collision frequency. A more mundane explanation is as N increases, the layer mass becomes significant with respect to the container mass. This reduces the change in layer velocity at impact and subsequently decreases the effective driving.

Finally, Fig. 15(b) looks at the effect of varying D on the grain mobility by plotting $C_{P_{max}}(4T)$ versus \tilde{v} for $D = 0.17, 0.33, 0.46$, and 0.66 (pressure data for constant \tilde{v} and varying N was not collected). The dependence of $C_{P_{max}}(4T)$ on \tilde{v} and the value of $\tilde{v}_{gm} \approx 3$ is in accord with the data for constant D and N and varying f shown in Fig. 13 and is consistent with our proposal that \tilde{v}_{gm} is independent of D . In addition to bronze, Fig. 15(b) also includes data for layers of lead and steel particles.

In summary, \tilde{v}_{gm} values obtained from local pressure measurements and from identifying the breakdown in wavelength scaling with H are in good qualitative agreement. Both show the same weak dependence on N for small Γ and

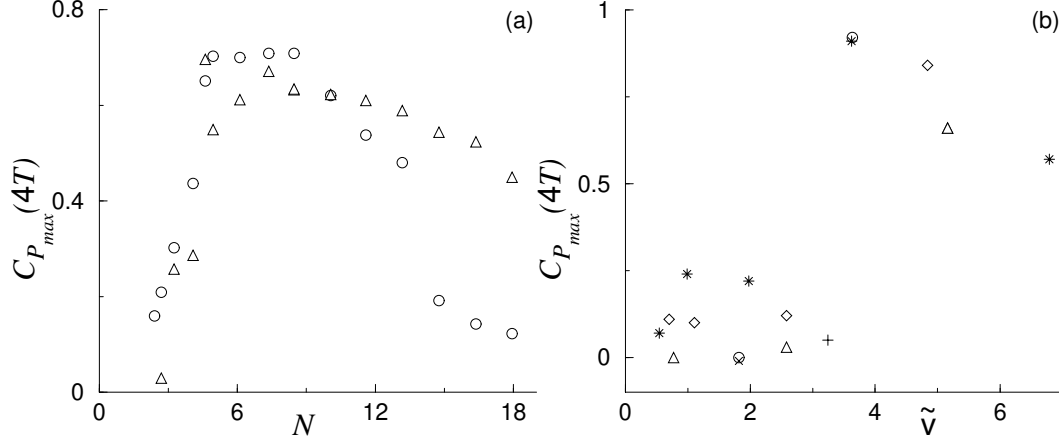


Fig. 15. (a) Autocorrelation of peak pressure versus N showing grain mobility transition at $N = 14$ for $\tilde{v} = 3.4$ (\circ) and absence of transition for $\tilde{v} = 4.2$ (\triangle) ($f = 30$ Hz). (b) Autocorrelation of peak pressure versus \tilde{v} illustrating the independence of grain mobility on D for D and N of 0.66 mm, 9 (\circ); 0.66 mm, 4 (\times); 0.33 mm, 9 (\diamond); 0.33 mm, 4 (\triangle); 0.46 mm lead, 3 ($+$); and 0.17 mm steel, 9 ($*$).

are independent of D . Quantitatively, the value of \tilde{v}_{gm} for $N < 12$ obtained from the dispersion data (≈ 2.6) is somewhat smaller than the value obtained from the local pressure fluctuations (≈ 3). A possible explanation for this discrepancy is the layer “freezes” from the bottom up as \tilde{v} is reduced. For $2.6 < \tilde{v} < 3.0$ the upper portion of the layer may be mobile but the associated mass variations are not seen in the pressure fluctuations because the variation in P is small relative to the inherent pressure noise associated with a flat layer and/or stress chains in the frozen portion of the layer wash out the pressure fluctuations by distributing them over an area comparable to or larger than λ .

7 Conclusion

Two length scales, the layer depth H and the particle diameter D , control the scaling properties of granular waves and granular wave patterns. As a guide, Table 2 provides a summary of the relevant dimensionless parameters and their associated transition values and figures. The horizontal mobility of grains appears to be determined by the container velocity — above a critical value $v_{gm} \approx 3\sqrt{Dg}$, grains are mobile while below v_{gm} , the layer depth remains uniform throughout the oscillation cycle. The physical mechanism responsible for the transition remains to be understood. The sharpness of the grain mobility transition stands in contrast to the gradual change in properties of gases as the length scale of disturbances approaches the mean free path. Additionally, it is surprising that finite grain size effects are made manifest via \tilde{v} rather than H/D or λ/D as mentioned in Sec. 5.

Table 2

Summary of parameters, transitions and associated figures.

Symbol	Description	Value	Figures
Γ	Dimensionless Acceleration	$4\pi^2 Af^2/g$	—
Γ_c	Flat-layer/Waves Transition	2.2 ($\Gamma \downarrow$)	3–5
f^*	Dimensionless Frequency	$f\sqrt{H/g}$	5, 8, 9
f_{ss}^*	Square/Stripe Transition	0.33	1, 6, 7
\tilde{v}	Dimensionless Velocity	$2\pi Af/\sqrt{Dg}$	—
\tilde{v}_{gm}	Grain Mobility Transition	3 ($N < 13$)	10–15

For $v > v_{gm}$, the layer behaves as a continuum with λ and f scaling with H and $\sqrt{H/g}$, respectively. With this scaling, dispersion curves for different layer depth and particle size collapse onto the curve given by Eq. 2. The square/stripe transition for most parameter values occurs within the continuum regime ($v > v_{gm}$), depends simply on the layer depth H ($f_{ss}^* = f_{ss}\sqrt{H/g} \approx 0.33$), and shows no systematic dependence on Γ , N , D , or particle composition (for lead, bronze, and steel). We do not yet understand why $f_{ss}^* = 0.33$, but speculate it is perhaps related to the dynamic angle of repose. For $v < v_{gm}$, scaling with H fails. Within this regime, local pressure measurements support the idea that waves result from a bending of the grain layer (see Mujica *et al.* Ref. [20]), although there is a large discrepancy between our value of $\tilde{v}_{gm} \approx 3$ and that found by Mujica *et al.* — $\tilde{v}_{gm} \approx 0.6$. Possibly, our measurements indicate where horizontal grain mobility stops whereas the value reported by Mujica *et al.* represents the cessation of relative vertical motion as well. Another interesting question is the nature of stripe patterns above the grain mobility transition. Does wave scaling with H exist in this regime? Casual observations show that stripes above the transition have shorter spatial and temporal correlations than do stripes in the sloshing regime.

Finally, the flat-layer/waves transition occurs when the layer remains dilated after making contact with the plate. For decreasing Γ , this transition occurs at a nearly constant value of $\Gamma = 2.2$, which is independent of f and N . Associated with the onset of waves is a sudden decrease in the collision pressure. Possibly the least understood aspect of the flat-layer/waves transition is the causative connection between the dilation and the pattern.

There remain numerous unanswered questions concerning wave patterns in vertically oscillated granular layers. Increased computational power, better simulation techniques, improved measurement capabilities, and application of Navier-Stokes-like continuum equations [30] promise significant new insights into this system in particular and into the dynamics of granular media in general.

Acknowledgments

The authors thank Chris Bizon and Mark Shattuck for helpful comments, Dan Goldman for experimental assistance, and Francisco Melo for illuminating discussions. This research was supported by the Engineering Research Program of the Office of Basic Energy Sciences of the U.S. Department of Energy and by the U.S. National Science Foundation Division of International Programs (Chile).

References

- [1] H. M. Jaeger, S. R. Nagel, and R. P. Behringer, *Rev. Mod. Phys.* **68** (1996) 1259-1273.
- [2] F. Melo, P. B. Umbanhowar, and H. L. Swinney, *Phys. Rev. Lett.* **72** (1994) 172-175.
- [3] F. Melo, P. B. Umbanhowar, and H. L. Swinney, *Phys. Rev. Lett.* **75** (1995) 3838-3841.
- [4] P. B. Umbanhowar, F. Melo, and H. L. Swinney, *Physica A* **249** (1997) 1-9.
- [5] P. B. Umbanhowar, F. Melo, and H. L. Swinney, *Nature* **382** (1996) 793-796.
- [6] M. C. Cross and P. C. Hohenberg, *Rev. Mod. Phys.* **65** (1993) 851-1112.
- [7] John R. de Bruyn, C. Bizon, M. D. Shattuck, D. Goldman, J. B. Swift, and H. L. Swinney, *Phys. Rev. Lett.* **81** (1998) 1421-1424.
- [8] A. Kudrolli and J. P. Gollub, *Physica D* **97** (1996) 133-154.
- [9] J. T. Jenkins and M. W. Richman, *Arch. Rat. Mech. Anal.* **87** (1985) 355-377.
- [10] C. Bizon, M. D. Shattuck, J. R. de Bruyn, J. B. Swift, W. D. McCormick, and H. L. Swinney, *J. Stat. Phys.* **93** (1998) 449-465.
- [11] C. Bizon, M. D. Shattuck, J. B. Swift, and H. L. Swinney, *Phys. Rev. E* **60** (1999) 4340-4351.
- [12] T. Shinbrot, *Nature* **389** (1997) 574-576; E. Cerda, F. Melo, and S. Rica, *Phys. Rev. Lett.* **79** (1997) 4570-4573; D. H. Rothman, *Phys. Rev. E* **57** (1998) R1239-R1242.
- [13] L. S. Tsimring and I. S. Aranson, *Phys. Rev. Lett.* **79** (1997) 213-216; H. Sakaguchi and H. R. Brand, *Physica D* **117** (1998) 95-105; J. Eggers and H. Riecke, *Phys. Rev. E* **59** (1999) 4476-4483.
- [14] S. C. Venkataramani and E. Ott, *Phys. Rev. Lett.* **80** (1998) 3495-3498.

- [15] S. Luding, E. Clément, J. Rajchenbach, and J. Duran, Europhys. Lett. **36** (1996) 247-252; K. M. Aoki and T. Akiyama, Phys. Rev. Lett. **77** (1996) 4166-4169; C. Bizon et al., ibid. **79** (1997) 4713; K. M. Aoki and T. Akiyama, ibid. **79** (1997) 4714.
- [16] C. Bizon, M. D. Shattuck, J. B. Swift, W. D. McCormick, and H. L. Swinney, Phys. Rev. Lett. **80** (1998) 57-60.
- [17] P. B. Umbanhowar, "Wave Patterns in Vibrated Granular Layers," Ph.D. Dissertation, The University of Texas at Austin, 1996.
- [18] Although the sensor diameter is less than λ for most of the data reported in Sec. 3, repeated runs over different and/or time varying patterns allow effective spatial averages to be obtained which are in quantitative agreement with global pressure measurements from Refs. [19,20].
- [19] N. Mujica and F. Melo, Phys. Rev. Lett. **80** (1998) 5121-5124.
- [20] N. Mujica and F. Melo, arXiv.org preprint, cond-mat/9905380 (1999).
- [21] In all experimental runs where Γ is varied, $d\Gamma/dt \approx 0.002f$, a rate at which the measured quantities are unchanged by further reduction of $d\Gamma/dt$.
- [22] Anita Mehta and J. M. Luck, Phys. Rev. Lett. **65** (1990) 393-396.
- [23] One might also argue that above $f^* = 0.4$ $\Gamma_{c\downarrow}$ and $\Gamma_{c\uparrow}$ exhibit the same dependence on f but with an offset. If correct, this observation may be related to the solid-like properties of the wave state above the grain mobility transition (see Sec. 6).
- [24] T. H. Metcalf, J. B. Knight and H. M. Jaeger, Physica A **236** (1997) 202-210.
- [25] E. Clément, L. Vanel, J. Rajchenbach, and J. Duran, Phys. Rev. E **53** (1996) 2972-2975.
- [26] For $\Gamma = 3.0$, no obvious departure from the collapse curve is evident for $N > 11$ since λ is near its limiting value of H .
- [27] The constant value of P_{max}^* for $\tilde{v} > 2.6$ can be interpreted as implying that the pattern amplitude A_p is proportional to $1/f^2$. Writing $P_{max}^* \propto v_{coll}/gt_{coll}$ and setting $t_{coll} = A_p/v_{coll}$ gives $A_p \propto v_{coll}^2/gP_{max}^* \propto 1/f^2$ since P_{max}^* is constant.
- [28] A related idea for grain mobility was proposed in Ref. [17] in terms of the average layer dilation per particle.
- [29] The results for the autocorrelation of the maximum pressure do not depend on this specific delay (*e.g.* $4T$). Other delay values less than $\approx 8T$ give the same results.
- [30] M. D. Shattuck, C. Bizon, J. B. Swift and Harry L. Swinney, Physica A, in press.